

Article

Exotic Cores with and without Dark-Matter Admixtures in Compact Stars

Rico Zöllner  and Burkhard KämpferHelmholtz-Zentrum Dresden Rossendorf & Institut für Theoretische Physik, TU Dresden,
01465 Dresden, Germany; kaempfer@hzdr.de

* Correspondence: rico@hierbeizoellners.de

Abstract: We parameterize the core of compact spherical star configurations by a mass (m_x) and a radius (r_x) and study the resulting admissible areas in the total-mass–total-radius plane. The employed fiducial equation-of-state models of the corona at radii $r > r_x$ and pressures $p \leq p_x$ with $p(r = r_x) = p_x$ are that of constant sound velocity and a proxy of DYΔ DD-ME2 provided by Buchdahl’s exactly solvable ansatz. The core ($r < r_x$) may contain any type of material, e.g., Standard-Model matter with unspecified equation of state or/and an unspecified Dark-Matter admixture. Employing a toy model for the cool equation of state with first-order phase transition, we also discuss the mass-radius relation of compact stars with an admixture of Dark Matter in a Mirror-World scenario.

Keywords: compact stars; mass-radius relation; equation of state; dark-matter admixtures



Citation: Zöllner, R.; Kämpfer, B. Exotic Cores with and without Dark-Matter Admixtures in Compact Stars. *Astronomy* **2022**, *1*, 36–48. <https://doi.org/10.3390/astronomy1010005>

Academic Editor: Ignatios Antoniadis

Received: 30 March 2022

Accepted: 24 May 2022

Published: 29 May 2022

Publisher’s Note: MDPI stays neutral with regard to jurisdictional claims in published maps and institutional affiliations.



Copyright: © 2022 by the authors. Licensee MDPI, Basel, Switzerland. This article is an open access article distributed under the terms and conditions of the Creative Commons Attribution (CC BY) license (<https://creativecommons.org/licenses/by/4.0/>).

1. Introduction

The advent of detecting gravitational waves from merging neutron stars, the related multi-messenger astrophysics [1–8] and the improving mass-radius determinations of neutron stars, in particular by NICER data [9–11], stimulated a wealth of activities. Besides mass and radius, moments of inertia and tidal deformabilities become experimentally accessible and can be confronted with theoretical models [1,12–18]. The baseline of the latter ones is provided by non-rotating, spherically symmetric cold dense matter configurations. The sequence of white dwarfs (first island of stability) and neutron stars (second island of stability) and—possibly [19]—a third island of stability [20–22] thereby shows up when moving to more compact objects, with details depending sensitively on the actual equation of state (EoS). The quest for a fourth island has been addressed too [23,24]. Here, “stability” means the damping of radial disturbances. Since the radii of configurations of the second (neutron stars) and third (hypothetical quark/hybrid stars [25–27]) islands are very similar, the notion of twin stars [28,29] has been coined for equal-mass configurations; “masquerade” was another related term [30].

The standard modeling of such static compact star configurations is based on the Tolman–Oppenheimer–Volkov (TOV) equations

$$\frac{dp}{dr} = -G_N \frac{(e+p)(m+4\pi pr^3)}{r^2(1-\frac{2G_N m}{r})}, \quad (1)$$

$$\frac{dm}{dr} = 4\pi er^2, \quad (2)$$

emerging from the energy–momentum tensor of a perfect isotropical fluid and spherical symmetry of space–time and matter as well, within the framework of Einstein gravity without a cosmological term. Newton’s constant is denoted by G_N , natural units with $c = 1$ are used, unless relating mass and length and energy density, for which $\hbar c$ is needed. Given a unique relationship of pressure p and energy density e as equation of state (EoS) $e(p)$, in particular at zero temperature, the TOV equations are integrated with boundary

conditions $p(0) = p_c$ and $m(0) = 0$ (implying $p(r) = p_c - \mathcal{O}(r^2)$ and $m(r) = 0 + \mathcal{O}(r^3)$ at small radii r), and $p(R) = 0$ and $m(R) = M$ with R as circumferential radius and M as gravitational mass (acting as a parameter in the external (vacuum) Schwarzschild solution at $r > R$). The quantity p_c is the central pressure. The solutions $R(p_c)$ and $M(p_c)$ provide the mass-radius relation in parametric form $M(R)$.

A great deal of effort is presently focused on the EoS at supra-nuclear densities [31]. Figure 1 in [32] exhibits the currently admitted uncertainty: up to a factor of ten in pressure as a function of energy density. At asymptotically large energy-density, perturbative QCD constrains the EoS, though it is just the non-asymptotic supra-nuclear density region which crucially determines whether twin stars may exist or quark-matter cores appear in neutron stars. Accordingly, one can fill this gap with a big number of test EoSs to scan through the possibly resulting mass-radius curves; see [33–36]. However, the option that neutron stars can accommodate Dark Matter (or other exotic material) [37–40] obscures the safe theoretical modeling of a reliable mass-radius relation in such a manner. Of course, inverting the posed problem with sufficiently precise data of masses and radii as input offers a promising avenue towards determining the EoS [33,41–46].

Here, we pursue another perspective: we parameterize the supra-nuclear core by a radius r_x and the included mass m_x and integrate the above TOV equations only in the corona, i.e., from pressure p_x to the surface, where $p = 0$. This yields the total mass $M(r_x, m_x; p_x)$ and the total radius $R(r_x, m_x; p_x)$ by assuming that the corona EoS $e(p)$ is reliably known at $p \leq p_x$. (Our notion “corona” could be substituted by “mantel” or “crust” or “envelope”. It refers to the complete part of the compact star outside the core, $r_x \leq r \leq R$.) Clearly, without knowledge of the matter composition at $p > p_x$ (may it be Standard-Model matter with uncertain EoS or may it contain a Dark-Matter admixture, for instance, or monopoles or some other type of “exotic” matter) one does not get a simple mass-radius relation by such procedure, but admissible area(s) over the mass-radius plane, depending on the core parameters r_x and m_x . This is the price of avoiding a special model of the core matter composition.

We are going to test two models of the corona EoS: (i) constant sound velocity with crucial parameter $e_0 = e(p = 0)$ and $p = 0$ for $e < e_0$, and (ii) Buchdahl’s EoS which, surprisingly, represents a proxy of the DYΔ DD-ME2 EoS [23] and has the property $\lim_{p \rightarrow 0} e(p) \rightarrow 0$. One could consider this as a test of the sensitivity against variations of the neutron star crust (see [47,48] for such a crust test within the traditional approach with a given core EoS).

We emphasize the relation of ultra-relativistic heavy-ion collision physics, related to the EoS $p(T, \mu_B \approx 0)$, and compact star physics, related to $p(T \approx 0, \mu_B)$, when focusing on static compact-star properties [49,50]. (Of course, in binary or ternary compact-star merging-events, finite temperatures T and a large range of baryon-chemical potential μ_B are also probed [51].) Implications of the conjecture of a first-order phase transition at small temperatures and large baryo-chemical potentials or densities [52–55] can be studied by neutron-hybrid-quark stars [56–59]. It has been known for some time [20–22,60,61] that a cold EoS with special pressure–energy-density relation $p(e)$, e.g., a strong local softening up to first-order phase transition with a density jump, can give rise to a “third family” of compact stars, beyond white dwarfs and neutron stars. In special cases, the third-family stars appear as twins of neutron stars [30,62,63]. Various scenarios of the transition dynamics to the denser configuration as mini-supernova were discussed quite early [64,65].

Our paper is organized as follows. In Section 2, we employ the corona EoS model (i) (constant sound velocity) and also consider the instructive limiting case of an incompressible fluid. Special relations of $m_x(r_x)$ are deployed to emphasize the relation to the traditional approach, which emerges as cut in the M - R plane representing the curve $M(R)$. Section 3 uses the corona EoS model (ii) (Buchdahl’s EoS as proxy of a nuclear-physics-based EoS). The $M(R)$ relations for models (i) and (ii) are quite different, as are the admitted areas over the M - R plane. We conclude in Section 4. Appendix A considers Dark-Matter or Mirror-World admixtures in neutron (quark) stars with a phase transition with the goal of

illustrating the potential impact of a first-order phase transition on the mass–radius relation and the quest for twin stars. This is another way to specify the relation $m_x(r_x)$.

2. Corona with Constant Sound Velocity EoS

The constant sound velocity EoS

$$p(e) = v_s^2(e - e_0) \text{ for } e > e_0, \quad p = 0 \text{ for } e \leq e_0 \quad (3)$$

introduces a scale setting parameter e_0 , which drops out in the representation by scaled quantities: $\bar{p} = p/e_0$, $\bar{r} = r\sqrt{G_N e_0}$, $\bar{m} = mG_N\sqrt{G_N e_0}$. Only the sound velocity $v_s^2 = \partial p/\partial e$ remains as parameter. We use this as model (i) and—arbitrarily—take $\bar{p}_x = 1$ as the upper limit of scaled pressure of the corona EoS.

2.1. A Limiting Case: Infinite Sound Velocity

It is instructive to consider the limiting case $v_s^{-2} \rightarrow 0$, i.e., $\bar{e} \rightarrow 1$ for $\bar{p} \leq 1$. The constant energy density in Equation (2) results in $\bar{m} = \bar{m}_x + \frac{4\pi}{3}(\bar{r}^3 - \bar{r}_x^3)$, and the Riccati-type ordinary differential Equation (1) becomes, by a suitable shift of the pressure, a Bernoulli equation, allowing a quadrature to get the pressure profile $\bar{p}(\bar{r}) = -1 + (\bar{p}_c + 1) \exp\{\frac{1}{2}(\lambda - \lambda_0)N\}$, $N^{-1} = 1 + 4\pi(\bar{p}_c + 1) \exp\{-\frac{1}{2}\lambda_0\} \int_{\bar{r}_x}^{\bar{r}} d\bar{r} \bar{r} \exp\{\frac{3}{2}\lambda(\bar{r})\}$, $e^{-\lambda} = 1 - 2\bar{m}/\bar{r}$, $\lambda_0 = \lambda(\bar{r}_x)$, cf. [22,66]. Since the term with $\int_{\bar{r}_x}^{\bar{r}} d\bar{r} \bar{r} \exp\{\frac{3}{2}\lambda(\bar{r})\}$ is less transparent due to the elliptic integral(s), we turn on an approximation of the case $e = \text{const}$ and numerically integrate Equations (1) and (2) with $v_s^{-2} = 10^{-4}$ to mimic the above constant energy density EoS by a proxy with large sound velocity. We then find admissible area in the \bar{M} - \bar{R} plane displayed in Figure 1. That area is mapped out here by curves $\bar{r}_x = \text{const}$ with \bar{m}_x varying from small (at the r.h.s.) to large (at the l.h.s.) values. The l.h.s. limitation is given by the black hole condition $\bar{M} = \bar{R}/2$ (red fat line). In the limit of small cores, the $\bar{r}_x = \text{const}$ curves $\bar{M} = \bar{m}_x + \frac{4\pi}{3}\bar{R}^3 - \mathcal{O}(r_x^3)$ approach the Schwarzschild mass–radius relation $\bar{M} = \frac{4\pi}{3}\bar{R}^3$ (dashed black curve), i.e., the gap to the $\bar{r}_x = \text{const}$ curve becomes larger with decreasing values of \bar{R} due to increasing \bar{m}_x . The Schwarzschild curve terminates in the asterisk, since that is where $\bar{p}_c = 1$ is reached. One may recall the pressure profile of the interior Schwarzschild solution $\bar{p}_{\text{Schwarz}}(\bar{r}) = -[(1 + \bar{p}_c) - (1 + 3\bar{p}_c)W]/[3(1 + \bar{p}_c) - (1 + 3\bar{p}_c)W]$, $W := \sqrt{1 - \frac{8\pi}{3}\bar{r}^2}$, yielding $\bar{R}(\bar{p}_c)$ from $\bar{p}(\bar{R}) = 0$ to see this via our proposition $\bar{p} \leq \bar{p}_x$.

In this context, it is interesting to compare the pressure profiles of the interior Schwarzschild solution and the core–corona model at small values of \bar{r}_x . Adjusting the central pressure of the interior Schwarzschild solution to obtain the same scaled radius \bar{R} as in the core–corona model with a given small value of \bar{r}_x and a given value of \bar{m}_x , one finds (not displayed) a rapidly dropping pressure in a narrow region above \bar{r}_x towards the Schwarzschild pressure $\bar{p}_{\text{Schwarz}}(\bar{r})$, which holds until the surface. In such a way, the admissible area of masses and radii of the core–corona model are bracketed by the black-hole limit at l.h.s. and the conventional mass–radius curve in the lower part of the mass–radius plane.

Let us now consider two possible sections through the mass–radius plane. First, we assume a core-mass vs. core-radius relation as $\bar{m}_x(\bar{r}_x) = \frac{4\pi}{3}\bar{r}_x^3$. This yields the dotted curve, which clearly coincides with the Schwarzschild relation when continuing the latter one to central pressures larger than \bar{p}_x . Note that with increasing values of \bar{r}_x , the admissible region of the core–corona model leaks increasingly into the r.h.s.

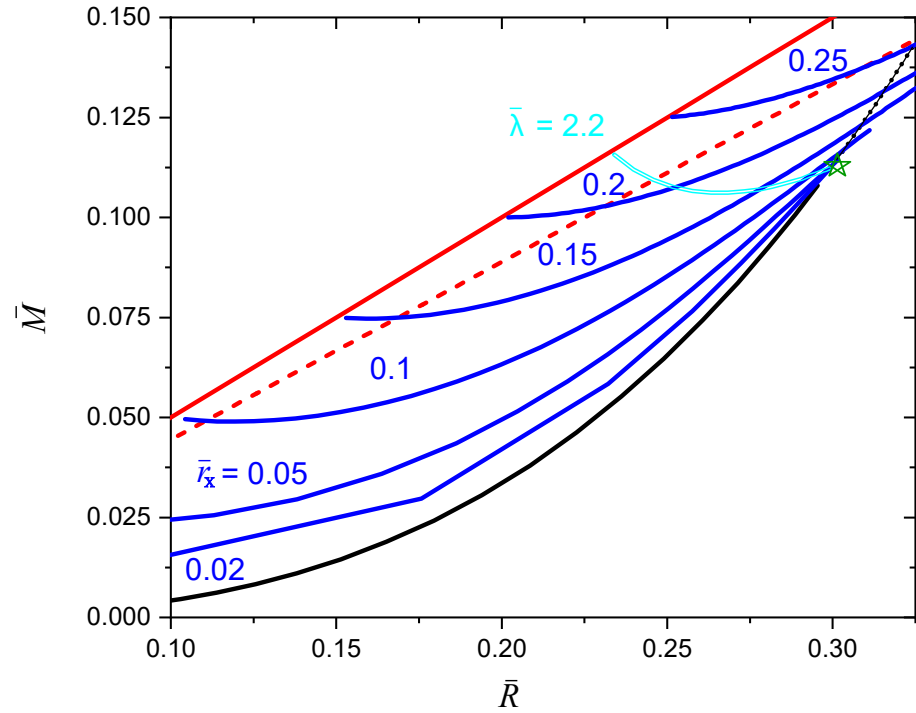


Figure 1. Admissible area in the \bar{M} - \bar{R} plane mapped out by curves $\bar{r}_x = \text{const}$ (blue solid, obtained by integrating the TOV equations from \bar{r}_x to \bar{R}). The black hole condition $\bar{M} = \bar{R}/2$ is depicted by the red fat line. Buchdahl's limit $\bar{M} = 4\bar{R}/9$ is displayed by the dashed red line. The Schwarzschild curve $\bar{M} = \frac{4\pi}{3}\bar{R}^3$ (black curve) terminates in the asterisk \star , where $\bar{p}_c = 1$ is reached. Allowing for a larger central pressure, the Schwarzschild curve continues (dotted black curve), which coincides with the core–corona model for $\bar{m}_x(\bar{r}_x) = \frac{4\pi}{3}\bar{r}_x^3$. Imposing the side condition $\bar{m}_x(\bar{r}_x) = \frac{4\pi}{3}\bar{\lambda}\bar{r}_x^3$ results in $\bar{\lambda} = 2.2$ in the cyan double curve. The actual calculations are for Equations (1)–(3) with $v_s^{-2} = 10^{-4}$, to approximate an EoS with constant energy-density.

A second side condition in relating the core-mass and core-radius is given by $\bar{m}_x(\bar{r}_x) = \frac{4\pi}{3}\bar{\lambda}\bar{r}_x^3$, meaning that the energy density in the core is $\bar{\lambda}$ times the energy density of the corona. (This is essentially the two-shell model considered in [21,22]). Selecting $\bar{\lambda} = 2.2$ facilitates the cyan double curve, again a well-defined mass–radius curve. Larger (smaller) values of $\bar{\lambda}$ bend down (up) that curve. The section between the local r.h.s. mass maximum at the asterisk and the local mass minimum belongs to unstable configurations, while left to the local mass minimum, the configurations become stable again. This very construction is at the heart of twin stars, i.e., stable configurations with the same mass but (slightly) different radii. There is notable leakage into the region l.h.s. to the Buchdahl bound (cf. [67] for a corollary) given by $\bar{M} = 4\bar{R}/9$. This issue is caused by the fact that a central pressure $\bar{p}_c < \infty$ does not drop to \bar{p}_x at radius \bar{r}_x when using the TOV equations with core density $\bar{\lambda}\bar{\epsilon}_0$. Phrased differently, the above ad hoc choice $\bar{m}_x(\bar{r}_x) = \frac{4\pi}{3}\bar{\lambda}\bar{r}_x^3$ is compatible with the TOV equations only for a limited range of values of \bar{r}_x . The validity of the TOV equations for a consistent (always decreasing) pressure profile from p_c to zero limits the extension of the curve under discussion and lets it terminate before reaching Buchdahl's limit. Nevertheless, extensions of the TOV equations, e.g., as system describing a multi-fluid medium with Dark-Matter components (see Appendix A), make the occupancy of the region beyond Buchdahl's limit conceivable.

2.2. Finite Sound Velocity

For a finite sound velocity, the mass–radius curve bends to the left and facilitates a mass maximum, e.g., $\bar{M}_{max} = 0.051$ at radius $\bar{R} = 0.195$ for $v_s^{-2} = 3$. By the requirement of

$M \approx 2M_\odot$ one gets $e_0 \approx 231.5 \text{ MeV}/\text{fm}^3$ and finds, from $R = MG_N \bar{R}/\bar{M}$, a radius of 11.27 km, (accidentally) in the right ballpark.

The mass–radius plane is exhibited in Figure 2 with the same line style conventions as in Figure 1. One meets the features discussed in the previous Subsection. The admissible region is bracketed l.h.s. by the black hole condition and r.h.s. by the plain mass–radius curve $\bar{M}(\bar{R})$ (dashed black curve) up to the asterisk, where $\bar{p}_c = \bar{p}_x$ is reached. In the dotted section, the central pressures obey $\bar{p}_c > \bar{p}_x$. Due to non-zero matter compressibility, the analog relation $\bar{m}_x(\bar{r}_x)$, discussed in Section 2.1, must be constructed numerically to see that this side condition within the core–corona model in fact coincides with the mass–radius curve obtained by the (ad hoc) continuation of the EoS (3) at $p > p_x$. For small values of $\bar{r}_x = \text{const}$, the permitted masses as a function of radius approach the mass–radius curve $\bar{M}(\bar{R})$. For larger constant values of \bar{r}_x , the pattern of the curves $\bar{M}(\bar{R}, \bar{r}_x, \bar{m}_x; \bar{p}_x)$ is as discussed in Section 2.1. They also leak beyond the Buchdahl limit.

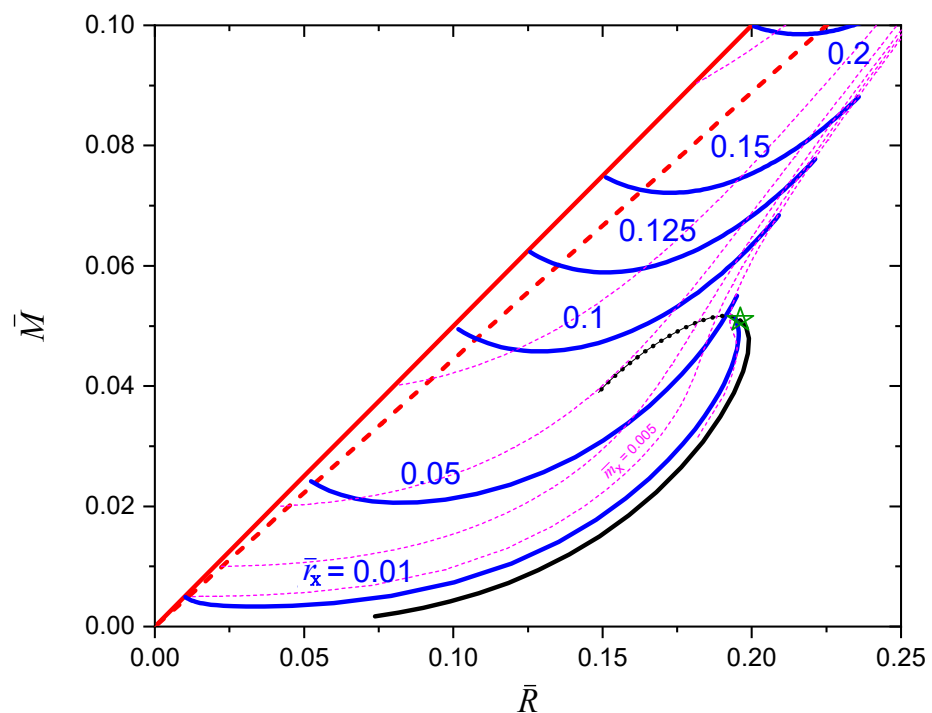


Figure 2. Same as Figure 1 but for $v_s^{-2} = 3$ to cope with causality. The dashed magenta curves depict additional mass–radius relations for running values of \bar{r}_x and $\bar{m}_x = \text{const}$ with values of 0.01, 0.02, 0.04, and 0.09 above the labeled $\bar{m}_x = 0.005$ curve; the rightmost curve for $\bar{m}_x = 0.001$ is displayed only for $\bar{M} > 0.03$.

We relegate the consideration of special cuts $\bar{m}_x(\bar{r}_x)$ and variations of p_x to the Appendix A, where we explicitly include an admixture of Dark Matter to be dealt within a two-fluid approach.

3. Corona with Buchdahl’s EoS and NYΔ DD-EM2

While the employed corona EoS in Section 2.2 displays a finite positive slope of the mass–radius curve for a large range, the currently preferred EoS models point to a steep increase. An example of an EoS compatible with neutron star data is NYΔ, based on the DD-ME2 density functional [23]. Surprisingly, Buchdahl’s EoS [68]

$$e = 12\sqrt{p_* p} - 5p, \quad p \leq p_* \tag{4}$$

with $p_* \approx 64 \text{ MeV}/\text{fm}^3$ matches fairly well NYΔ within the range tabulated in [23], see Table 1. Due to causality requirement $v_s^2 \leq 1$, Equation (4) is limited to $p \leq p_*$. In contrast to the EoS of model (i), Equation (4) extends smoothly to $e = 0$ and $p = 0$. The mass–radius

relation is given by $M = \beta R/G_N$, and the radius is parameterized by $R = \frac{1-\beta}{\sqrt{1-2\beta}} \sqrt{\frac{\pi}{288p_*G_N}}$ for $\beta \in [0, 1/6]$ [68,69]. In this section, we use physical units, e.g., p_* in MeV/fm^3 instead of \bar{p}_x , and display masses in units of M_\odot and radii in units of km. With the above quoted value of p_* one finds $R = 11.33 \frac{1-\beta}{\sqrt{1-2\beta}}$ km and $M = 7.66\beta \frac{1-\beta}{\sqrt{1-2\beta}} M_\odot$, where the maximum mass $1.31M_\odot$ and radius 11.56 km can be read off.

The resulting mass–radius plot is exhibited in Figure 3, with line style conventions as seen in Figure 1. All the features discussed in Section 2 are recovered, e.g., the convex shape of the curves $r_x = \text{const}$, the approach of these curves to the mass–radius relation based on the EoS (4) at small values of r_x , the occupancy of a region beyond the Buchdahl limit up to the black hole limit etc. Since $p_x = p_*$ is comparatively small, the resulting mass–radius curve (solid black curve) terminates at rather small mass, quoted above. However, the core–corona decomposition shows that the maximum-mass region of NY Δ -DD-ME2 (see gray curves) is easily uncovered too, interestingly with sizeable core radii and noticeably smaller up to larger total radii.

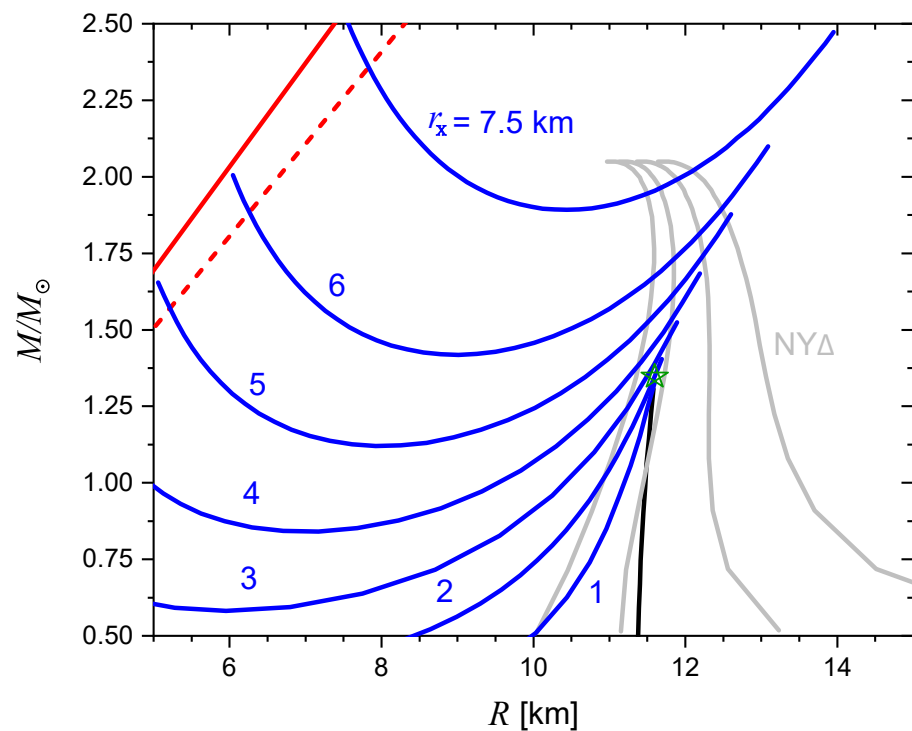


Figure 3. Same as Figure 1, however for the corona model (ii), i.e., EoS (4) with $p_* = 64 \text{ MeV}/\text{fm}^3$ (solid black curve). Note the different units. Faint gray curves are based on the standard integration of the TOV equations by using the numbers of the NY Δ EoS tabulated in [23] with linear interpolation both in between the mesh and from the tabulated minimum energy density to the $p = 0$ point at e_0 . The chosen values are $e_0 = 100, 10, 1,$ and $0.1 \text{ MeV}/\text{fm}^3$ (from left to right). The variation of the low-mass sections of these mass–radius curves points to some sensitivity on the outer crust properties. The slight deviation of the solid black curve and the second (from left) gray curve points to a non-perfect match of (4) and NY Δ .

4. Summary

We investigate a scenario which assumes the knowledge of a trustable equation of state (EoS) for compact spherical stars at pressures $p \leq p_x$. In a core–corona decomposition, the core with an unspecified composition and thus unknown (maybe exotic matter) equation(s) of state is parameterized by a mass m_x and a radius r_x ; the pressure at r_x is just p_x . Besides the unspecified equations of state at $p > p_x$, the core may also contain any type of matter, most notably Dark Matter. By definition, outside the core—in the

corona—only a Standard-Model neutron-star matter is present, described by the fiducial (“trustable”) EoS. The solution of the TOV equations of the corona pressure profile $p(r)$ for radii $r \geq r_x$ delivers a broad range of admissible masses and radii of the total core–corona configurations, bracketed by the black hole limit (thus going beyond the Buchdahl limit) and, in part, by the conventional mass–radius curve. We explore these admissible regions by using two test EoS models of the corona as simple substitutes of a state-of-the-art EoS: one with a constant sound velocity EoS and another one which refers to Buchdahl’s EoS, which in turn approximates some part of a particular density-functional approach, i.e., NYΔ DD-ME2. The latter is compatible with current mass–radius observations.

One may imagine that all possible continuations of a fiducial (“trustable”) EoS beyond p_x generate mass–radius curves within the admissible region, even with the Buchdahl limit as a border line. However, the admissible region is larger, since it can refer to cores which are not described by the isotropic one-fluid TOV equations. A straightforward extension of the latter is provided by the two-fluid TOV equations, dealt with in the Appendix. In line with investigations of the impact of the cool EoS on compact star properties, including the intriguing quest for twin stars, we add this schematic consideration of compact-star mass–radius relations for an EoS with first-order phase transition. In doing so, the two-fluid model is deployed where the second fluid is aimed at describing Dark Matter leaking out of a Mirror World. This scenario also facilitates the option of twin stars for a wide range of the Dark Matter admixture.

Author Contributions: Software, R.Z.; Supervision, B.K.; Writing—original draft, B.K.; Writing—review & editing, R.Z. All authors have read and agreed to the published version of the manuscript.

Funding: The work is supported in part by the European Union’s Horizon 2020 research and innovation program STRONG-2020 under grant agreement No 824093.

Institutional Review Board Statement: Not applicable.

Informed Consent Statement: Not applicable.

Data Availability Statement: Not applicable.

Acknowledgments: One of the authors (BK) acknowledges continuous discussions with J. Schaffner-Bielich and K. Redlich for the encouragement to deal (again) with the current topic.

Conflicts of Interest: The authors declare no conflict of interest.

Appendix A. Dark-Matter/Mirror-World Admixtures in Neutron Stars with Phase Transition

Spherical multi-fluid configurations in hydrostatic equilibrium are determined by the generalized TOV equations (cf. [70,71])

$$\frac{d\bar{p}^{(i)}}{d\bar{r}} = -(\bar{e}^{(i)} + \bar{p}^{(i)}) \frac{1}{r^2} \frac{\sum \bar{m}^{(i)} + 4\pi\bar{r}^3 \sum \bar{p}^i}{1 - 2\frac{\sum \bar{m}^{(i)}}{\bar{r}}}, \quad (\text{A1})$$

$$\frac{d\bar{m}^{(i)}}{d\bar{r}} = 4\pi\bar{r}^2 \bar{e}^{(i)}, \quad (\text{A2})$$

where the index i labels the fluid components, which are here assumed to be not mutually interacting but are governed by the common gravity field. The quantities are scaled commonly by e_0 , which figures in the EoS

$$\bar{p} = \begin{cases} 0 & \text{for } \bar{e} \leq 1, \\ v_s^2(\bar{e} - 1) & \text{for } 1 < \bar{e} < 1 + v_s^{-2}\bar{p}_x, \\ \bar{p}_x \dots \infty & \text{for } \bar{e} = \bar{\lambda}(1 + v_s^{-2}\bar{p}_x). \end{cases} \quad (\text{A3})$$

The incompressible part at $\bar{p} \geq \bar{p}_x$ mimics a stiff EoS above the phase transition at \bar{p}_x with energy density jump $\bar{\lambda}$, i.e., $\Delta\bar{e} = (\bar{\lambda} - 1)(1 + v_s^{-2}\bar{p}_x)$. Phrased differently, the EoS Equation (A3)

is a toy model of a linear EoS, $p = v_s^2(e - e_0)$ for $e \in (e_0, e_x)$, and $p = p_x + \hat{v}_s^2(e - \lambda e_x)$ for $e \geq \lambda e_x$, where p_x and e_x are related by $p_x = v_s^2(e_x - e_0)$ [72]. To reduce the parameter space, we consider $\hat{v}_s^2 \rightarrow \infty$ as limiting stiffness. Due to deploying the scaled quantities, one gets rid of the explicit value of the surface energy-density e_0 , where $p(R) = 0$ holds.

Fluid $i = 1$ is attributed to Standard-Model matter (SM) and should represent dense strong-interaction (hadron ... quark) matter in β equilibrium with local electric charge neutrality. Fluid $i = 2$ stands for a non-self-annihilating Dark-Matter (DM) candidate, which we also describe using Equation (A3), i.e., $\bar{p}^{(i)}(\bar{e}^{(i)})$ has the same functional dependence for all i , thus tremendously reducing the parameter space. What now distinguishes SM and DM is the central pressure: $\bar{p}_c^{(1)}$ and $\bar{p}_c^{(2)}$ parameterize the solutions $\bar{p}^{(i)}(\bar{r}; \bar{p}_c^{(1)}, \bar{p}_c^{(2)})$ and $\bar{m}^{(i)}(\bar{r}; \bar{p}_c^{(1)}, \bar{p}_c^{(2)})$ of (A1)–(A3) yielding, e.g., $\bar{M} = \bar{M}^{(1)} + \bar{M}^{(2)}$ as total gravitational star mass and visible-matter circumferential radius $\bar{R} = \bar{R}^{(1)}$ for choices $\bar{p}_c^{(2)} = x\bar{p}_c^{(1)}$ with $x \in [0, 1]$, facilitating $\bar{R}^{(2)} \leq \bar{R}^{(1)}$.

One could also think on fluid $i = 2$ as matter in a hidden Mirror World which duplicates our SM world and communicates essentially only via gravity (cf. [73–75] for recent activities in the field founded fifty years ago [76]). Particles of the Mirror World apparently represent candidates of Dark Matter [77,78] (cf. [79–81] for further implications and [82–84] for cosmological aspects, including SM matter–DM portal/mixing/feeble-interaction issues). Such a picture justifies the application of the EoS, Equation (A3), for both SM matter and DM; see [85]. We emphasize that, in this Appendix, DM described by Equation (A3) is possible at all pressures $\bar{p} \gtrsim \bar{p}_x$, while in Section 2, no DM is allowed at $\bar{p} < \bar{p}_x$. To expose this difference, we contrast the EoSs used in Section 2 and in the current Appendix in Figure A1.

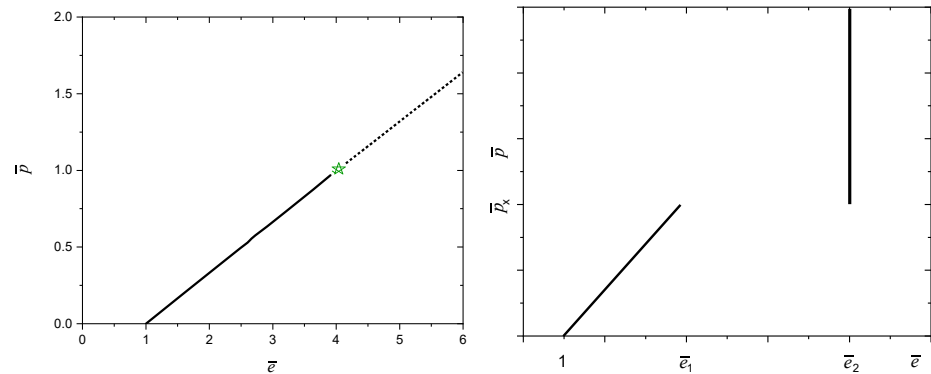


Figure A1. Schematic plots of the EoSs employed in Section 2 (left panel) and in the current Appendix (right panel). Left panel: Equation (3) for $v_s^{-2} = 3$ and $\bar{p}_x = 1$. The asterisk marks the endpoint of the fiducial SM matter EoS (solid black line, which is a substitute of a trustable EoS), resulting in the mass–radius curve exhibited in Figure 2 by the solid black curve. Beyond $\bar{p} = 1$, any EoS is conceivable. The dotted line is one possible extension of the fiducial EoS, especially with the same sound velocity. The resulting mass–radius relation is depicted in Figure 2 by the dotted black curve for Standard-Model matter only. Another conceivable continuation could be analog to the pattern displayed in the right panel. Right panel: Equation (A3) with $\bar{e}_0 = 1$ (by definition) and $\bar{e}_1 = \bar{e}_0 + v_s^{-2}\bar{p}_x$ and $\bar{e}_2 = \bar{\lambda}\bar{e}_1$. Several values of \bar{p}_x (here the critical pressure of a first-order phase transition) are considered, while $v_s^{-2} = 3$ and $\bar{\lambda} = 3$ are kept fixed. The same EoSs apply for SM matter and DM Mirror-World matter.

Numerical results, relying on regularity in the center, $\bar{m}^{(i)} = 0 + \mathcal{O}(\bar{r}^3)$, and boundary values $\bar{p}^{(i)} = \bar{p}_c^{(i)} - \mathcal{O}(\bar{r}^2)$ at $\bar{r} \rightarrow 0$, are exhibited in Figure A2 for $v_s^{-2} = 3$. (For the dependence on v_s^2 , see [86] (a factor of $\sqrt{197.32}$ is to be applied for \bar{M} and \bar{R} in Figure 7 there).) The solid black curves display the mass–radius relation for $\bar{p}_x \rightarrow \infty$, i.e., the constant sound velocity EoS is extended unlimited to high pressure (while in Section 2 it was restricted to $p \leq p_x$). Gradually reducing the value of \bar{p}_x means including an energy-density jump from

\bar{e}_x to $\bar{\lambda}\bar{e}_x$ at pressure \bar{p}_x (mimicking a sharp first-order phase transition). The mass–radius curves become strongly modified (see colored curves), since the density jump $\Delta\bar{e}$ is fairly large. In particular, for $\bar{p}_x \leq 1$, an unstable section of the mass–radius curve is caused, where the slope is negative, followed by a sequence of stable configurations, where the slope is positive again; see the respective Figure 2 in [87–89] for the very pattern of stable–unstable–stable branches. Equal-mass points on the stable sections represent twin stars. The case of $\bar{p}_c^{DM} \equiv \bar{p}_c^{(i=2)} = 0$ (left top panel, $x = 0$) corresponds to no DM at all, as in Figure 2, and exhibits various cuts provided by an implicit relation of $\bar{m}_x(\bar{r}_x)$. Thus, it directly supplements Figure 2.

With increasing DM fraction, parameterized by x , the pattern seen in the left top panel of Figure A2 ($x = 0$) is shifted to left-down, i.e., the configurations become more and more compact. A tiny admixture of DM, e.g., $x = 0.01$ (right top panel), does hardly have any noticeable impact on the mass–radius curves. For $x = 0.1$, one can recognize the left-down shift of the pattern, which becomes somewhat larger at $x = 0.2$; see middle row. The subtle interplay of \bar{p}_c and \bar{p}_c^{DM} and \bar{p}_x causes additional features at $x \approx 0.5$ due to slightly displaced jumps in the energy density profiles; see left bottom panel. The special value $x = 1$ means that SM matter and DM have the same pressure and energy-density profiles, i.e., $\bar{p}^{(i=1)}(\bar{r}) = \bar{p}^{(i=2)}(\bar{r})$ and $\bar{e}^{(i=1)}(\bar{r}) = \bar{e}^{(i=2)}(\bar{r})$ implying $\bar{m}^{(i=1)}(\bar{r}) = \bar{m}^{(i=2)}(\bar{r})$. The resulting configurations become most compact, as exhibited in the right bottom panel. For $p^{(i)}(r) = p(r)$ and $m^{(i)}(r) = m(r)$, the generalized Schwarzschild pressure profile in the uniform-density core of n mutually non-interacting fluids, with e_2 each, reads

$$p_{Schwarz,n}(r) = -e_2 \frac{(e_2 + p_c) - (e_2 + 3p_c)W_n}{3(e_2 + p_c) - (e_2 + 3p_c)W_n}, \quad (A4)$$

$$W_n(r) := \sqrt{1 - n \frac{8\pi}{3} G_N e_2 r^2}, \quad (A5)$$

where the scaling, e.g., by $e_2 = \bar{\lambda}(e_0 + v_s^{-2} p_x)$ when referring to the EoS (A3), can be applied. The core radius follows from $p_{Schwarz,n}(r) = p_x$; it scales as $\propto 1/\sqrt{n}$.

The selected range of \bar{p}_x causes a crossing of the mass–radius curves within narrow regions. This can be considered as reminiscence of the “special point” discussed in [59,90].

When relating these panels to Figure 2, one must ensure that, at radius \bar{r}_x , the DM component must have vanished. On account of that requirement, the panels in Figure A2 provide explicit examples of possible cuts in the mass–radius plane of Figure 2 under variation of \bar{p}_x . One could demonstrate this relation more explicitly by digging out the information of \bar{m}_x and \bar{r}_x along the mass–radius curves in Figure A2. We leave such a study for follow-up work.

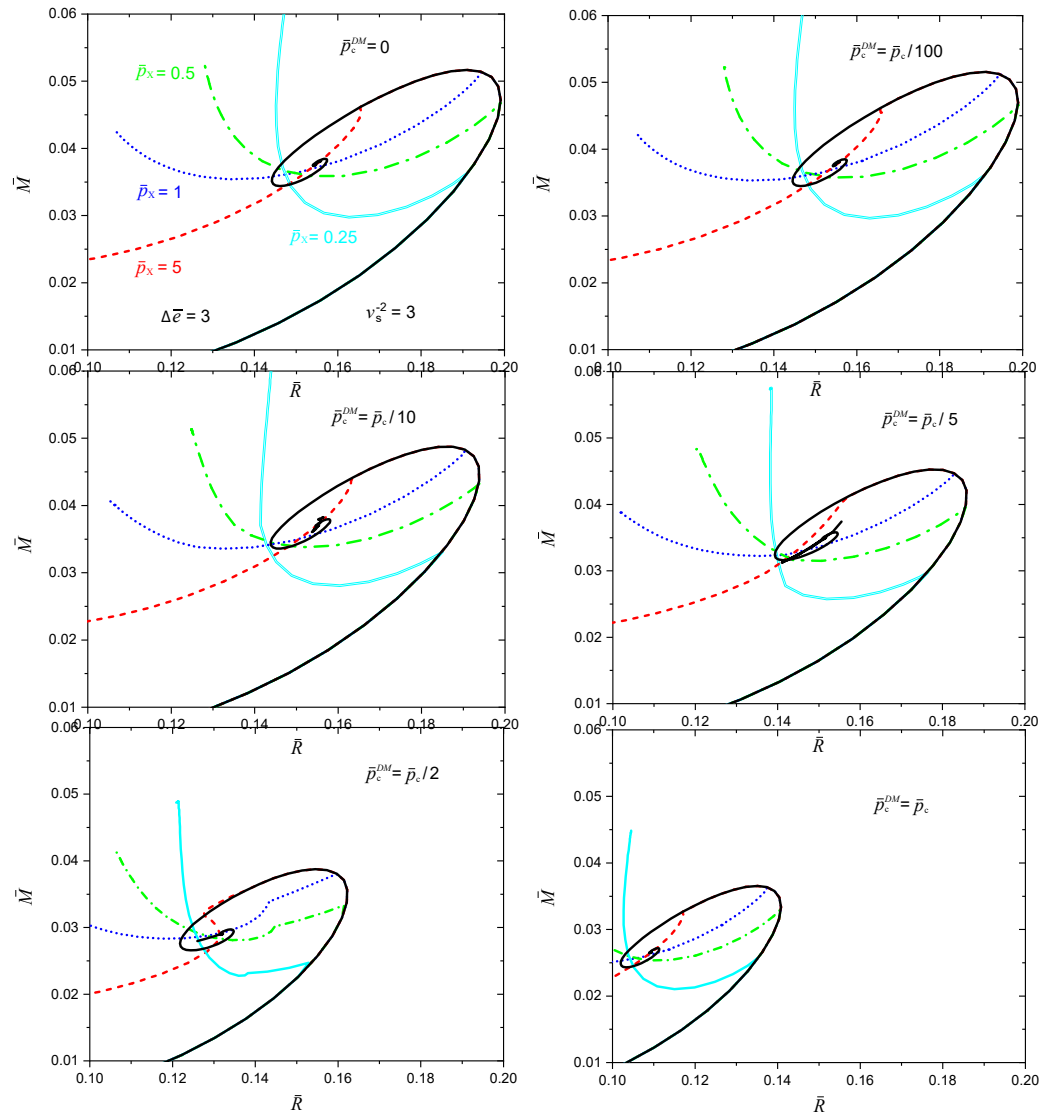


Figure A2. Mass–radius relations of neutron stars with Dark-Matter admixture for $v_s^{-2} = 3$ and $\Delta \bar{e}/\bar{e}_0 = 3$ and various values of $\bar{p}_x \equiv p_x/e_0$ (black solid: ∞ (i.e., no phase transition), cyan double line: 0.25, green dot-dashed: 0.5, blue dotted: 1, red dashed: 5). The equation of state Equation (A3) is used. The DM admixture is determined by the relation $\bar{p}_c^{DM} = x\bar{p}_c$ with $x = 0$ (left top panel, $\bar{r}_x^{DM} = \bar{m}_x^{DM} = 0$) to 1 (right bottom panel, $\bar{r}_x^{DM} = \bar{r}_x$, $\bar{m}_x^{DM} = \bar{m}_x$). The central pressures are very large towards the endpoints of curves terminating within the panels.

References

1. Pang, P.T.H.; Tews, I.; Coughlin, M.W.; Bulla, M.; Broeck, C.V.D.; Dietrich, T. Nuclear Physics Multimessenger Astrophysics Constraints on the Neutron Star Equation of State: Adding NICER’s PSR J0740+6620 Measurement. *Astrophys. J.* **2021**, *14*, 922.
2. Annala, E.; Gorda, T.; Katerini, E.; Kurkela, A.; Nättilä, J.; Paschalidis, V.; Vuorinen, A. Multimessenger constraints for ultra-dense matter. *Phys. Rev. X* **2022**, *12*, 011058.
3. Yu, J.; Song, H.; Ai, S.; Gao, H.; Wang, F.; Wang, Y.; Lu, Y.; Fang, W.; Zhao, W. Multimessenger Detection Rates and Distributions of Binary Neutron Star Mergers and Their Cosmological Implications. *Astrophys. J.* **2021**, *916*, 54.
4. Nicholl, M.; Margalit, B.; Schmidt, P.; Smith, G.P.; Ridley, E.J.; Nuttall, J. Tight multimessenger constraints on the neutron star equation of state from GW170817 and a forward model for kilonova light-curve synthesis. *Mon. Not. Roy. Astron. Soc.* **2021**, *505*, 3016–3032.
5. Margutti, R.; Chornock, R. First Multimessenger Observations of a Neutron Star Merger. *Ann. Rev. Astron. Astrophys.* **2021**, *59*, 155.
6. Tang, S.P.; Jiang, J.L.; Gao, W.H.; Fan, Y.Z.; Wei, D.M. Constraint on phase transition with the multimessenger data of neutron stars. *Phys. Rev. D* **2021**, *103*, 063026.
7. Tews, I.; Pang, P.T.H.; Dietrich, T.; Coughlin, M.W.; Antier, S.; Bulla, M.; Heinzel, J.; Issa, L. On the Nature of GW190814 and Its Impact on the Understanding of Supranuclear Matter. *Astrophys. J. Lett.* **2021**, *908*, L1.

8. Silva, H.O.; Holgado, A.M.; Cardenas-Avendano, A.; Yunes, N. Astrophysical and theoretical physics implications from multi-messenger neutron star observations. *Phys. Rev. Lett.* **2021**, *126*, 181101.
9. Riley, T.E.; Watts, A.L.; Ray, P.S.; Bogdanov, S.; Guillot, S.; Morsink, S.M.; Bilous, A.V.; Arzoumanian, Z.; Choudhury, D.; Deneva, J.S.; et al. A NICER View of the Massive Pulsar PSR J0740+6620 Informed by Radio Timing and XMM-Newton Spectroscopy. *Astrophys. J. Lett.* **2021**, *918*, L27.
10. Miller, M.C.; Lamb, F.K.; Dittmann, A.J.; Bogdanov, S.; Arzoumanian, Z.; Gendreau, K.C.; Guillot, S.; Ho, W.C.G.; Lattimer, J.M.; Loewenstein, M.; et al. The Radius of PSR J0740+6620 from NICER and XMM-Newton Data. *Astrophys. J. Lett.* **2021**, *918*, L28.
11. Miller, M.C.; Lamb, F.K.; Dittmann, A.J.; Bogdanov, S.; Arzoumanian, Z.; Gendreau, K.C.; Guillot, S.; Harding, A.K.; Ho, W.C.G.; Lattimer, J.M.; et al. PSR J0030+0451 Mass and Radius from NICER Data and Implications for the Properties of Neutron Star Matter. *Astrophys. J. Lett.* **2019**, *887*, L24.
12. Chatziioannou, K. Neutron star tidal deformability and equation of state constraints. *Gen. Rel. Grav.* **2020**, *52*, 109.
13. Christian, J.E.; Schaffner-Bielich, J. Twin Stars and the Stiffness of the Nuclear Equation of State: Ruling Out Strong Phase Transitions below $1.7n_0$ with the New NICER Radius Measurements. *Astrophys. J. Lett.* **2020**, *894*, L8.
14. Motta, T.F.; Thomas, A.W. The role of baryon structure in neutron stars. *Mod. Phys. Lett. A* **2022**, *37*, 2230001.
15. Jokela, N.; Järvinen, M.; Remes, J. Holographic QCD in the NICER era. *Phys. Rev. D* **2022**, *105*, 086005.
16. Kovensky, N.; Poole, A.; Schmitt, A. Building a realistic neutron star from holography. *Phys. Rev. D* **2022**, *105*, 034022.
17. Zhang, N.B.; Li, B.A. Impact of NICER's Radius Measurement of PSR J0740+6620 on Nuclear Symmetry Energy at Suprasaturation Densities. *Astrophys. J.* **2021**, *921*, 111.
18. Pereira, J.P.; Bejger, M.; Tonetto, L.; Lugones, G.; Haensel, P.; Zdunik, J.L.; Sieniawska, M. Probing elastic quark phases in hybrid stars with radius measurements. *Astrophys. J.* **2021**, *910*, 145.
19. Christian, J.E.; Schaffner-Bielich, J. Supermassive Neutron Stars Rule Out Twin Stars. *Phys. Rev. D* **2021**, *103*, 063042.
20. Gerlach, U.H. Equation of State at Supranuclear Densities and the Existence of a Third Family of Superdense Stars. *Phys. Rev.* **1968**, *172*, 1325.
21. Kämpfer, B. On the Possibility of Stable Quark and Pion Condensed Stars. *J. Phys. A* **1981**, *14*, L471.
22. Kämpfer, B. On stabilizing effects of relativity in cold spheric stars with a phase transition in the interior. *Phys. Lett. B* **1981**, *101*, 366.
23. Li, J.J.; Sedrakian, A.; Alford, M. Relativistic hybrid stars with sequential first-order phase transitions and heavy-baryon envelopes. *Phys. Rev. D* **2020**, *101*, 063022.
24. Alford, M.G.; Sedrakian, A. Compact stars with sequential QCD phase transitions. *Phys. Rev. Lett.* **2017**, *119*, 161104.
25. Malfatti, G.; Orsaria, M.G.; Ranea-Sandoval, I.F.; Contrera, G.A.; Weber, F. Delta baryons and diquark formation in the cores of neutron stars. *Phys. Rev. D* **2020**, *102*, 063008.
26. Pereira, J.P.; Bejger, M.; Zdunik, J.L.; Haensel, P. Differentiating sharp phase transitions from mixed states in neutron stars. *arXiv* **2022**, arXiv:2201.01217.
27. Bejger, M.; Blaschke, D.; Haensel, P.; Zdunik, J.L.; Fortin, M. Consequences of a strong phase transition in the dense matter equation of state for the rotational evolution of neutron stars. *Astron. Astrophys.* **2017**, *600*, A39.
28. Glendenning, N.K.; Kettner, C. Nonidentical neutron star twins. *Astron. Astrophys.* **2000**, *353*, L9.
29. Jakobus, P.; Motornenko, A.; Gomes, R.O.; Steinheimer, J.; Stoecker, H. The possibility of twin star solutions in a model based on lattice QCD thermodynamics. *Eur. Phys. J. C* **2021**, *81*, 41.
30. Alford, M.; Braby, M.; Paris, M.W.; Reddy, S. Hybrid stars that masquerade as neutron stars. *Astrophys. J.* **2005**, *629*, 969.
31. Reed, B.T.; Fattoyev, F.J.; Horowitz, C.J.; Piekarewicz, J. Implications of PREX-2 on the Equation of State of Neutron-Rich Matter. *Phys. Rev. Lett.* **2021**, *126*, 172503.
32. Annala, E.; Gorda, T.; Kurkela, A.; Nättilä, J.; Vuorinen, A. Evidence for quark-matter cores in massive neutron stars. *Nat. Phys.* **2020**, *16*, 907.
33. Ayriyan, A.; Blaschke, D.; Grunfeld, A.G.; Alvarez-Castillo, D.; Grigorian, H.; Abgaryan, V. Bayesian analysis of multimessenger M-R data with interpolated hybrid EoS. *Eur. Phys. J. A* **2021**, *57*, 318.
34. Oter, E.L.; Windisch, A.; Llanes-Estrada, F.J.; Alford, M. nEoS: Neutron Star Equation of State from hadron physics alone. *J. Phys. G* **2019**, *46*, 084001.
35. Lattimer, J.M.; Prakash, M. The Equation of State of Hot, Dense Matter and Neutron Stars. *Phys. Rept.* **2016**, *621*, 127.
36. Greif, S.K.; Hebeler, K.; Lattimer, J.M.; Pethick, C.J.; Schwenk, A. Equation of state constraints from nuclear physics, neutron star masses, and future moment of inertia measurements. *Astrophys. J.* **2020**, *901*, 155.
37. Anzuini, F.; Bell, N.F.; Busoni, G.; Motta, T.F.; Robles, S.; Thomas, A.W.; Virgato, M. Improved treatment of dark matter capture in neutron stars III: Nucleon and exotic targets. *J. Cosmol. Astropart. Phys.* **2021**, *11*, 056.
38. Bell, N.F.; Busoni, G.; Robles, S. Capture of Leptophilic Dark Matter in Neutron Stars. *J. Cosmol. Astropart. Phys.* **2019**, *06*, 054.
39. Das, H.C.; Kumar, A.; Kumar, B.; Patra, S.K. Dark Matter Effects on the Compact Star Properties. *Galaxies* **2022**, *10*, 14.
40. Das, H.C.; Kumar, A.; Patra, S.K. Dark matter admixed neutron star as a possible compact component in the GW190814 merger event. *Phys. Rev. D* **2021**, *104*, 063028.
41. Blaschke, D.; Ayriyan, A.; Alvarez-Castillo, D.E.; Grigorian, H. Was GW170817 a Canonical Neutron Star Merger? Bayesian Analysis with a Third Family of Compact Stars. *Universe* **2020**, *6*, 81.
42. Newton, W.G.; Balliet, L.; Budimir, S.; Crocombe, G.; Douglas, B.; Head, T.B.; Langford, Z.; Rivera, L.; Sanford, J. Ensembles of unified crust and core equations of state in a nuclear-multimessenger astrophysics environment. *Eur. Phys. J. A* **2022**, *58*, 69.

43. Huth, S.; Pang, P.T.H.; Tews, I.; Dietrich, T.; Fèvre, A.L.; Schwenk, A.; Trautmann, W.; Agarwal, K.; Bulla, M.; Coughlin, M.W.; et al. Constraining Neutron-Star Matter with Microscopic and Macroscopic Collisions. *arXiv* **2021**, arXiv:2107.06229
44. Raaijmakers, G.; Greif, S.K.; Hebeler, K.; Hinderer, T.; Nissanke, S.; Schwenk, A.; Riley, T.E.; Watts, A.L.; Lattimer, J.M.; Ho, W.C.G. Constraints on the Dense Matter Equation of State and Neutron Star Properties from NICER's Mass–Radius Estimate of PSR J0740+6620 and Multimessenger Observations. *Astrophys. J. Lett.* **2021**, *918*, L29.
45. Raaijmakers, G.; Riley, T.E.; Watts, A.L.; Greif, S.K.; Morsink, S.M.; Hebeler, K.; Schwenk, A.; Hinderer, T.; Nissanke, S.; Guillot, S.; et al. A NICER view of PSR J0030+0451: Implications for the dense matter equation of state. *Astrophys. J. Lett.* **2019**, *887*, L22.
46. Raaijmakers, G.; Greif, S.K.; Riley, T.E.; Hinderer, T.; Hebeler, K.; Schwenk, A.; Watts, A.L.; Nissanke, S.; Guillot, S.; Lattimer, J.M.; et al. Constraining the dense matter equation of state with joint analysis of NICER and LIGO/Virgo measurements. *Astrophys. J. Lett.* **2020**, *893*, L21.
47. Suleiman, L.; Fortin, M.; Zdunik, J.L.; Haensel, P. Influence of the crust on the neutron star macrophysical quantities and universal relations. *Phys. Rev. C* **2021**, *104*, 015801.
48. Lattimer, J.M.; Prakash, M. Neutron Star Observations: Prognosis for Equation of State Constraints. *Phys. Rept.* **2007**, *442*, 109.
49. Klahn, T.; Blaschke, D.; Typel, S.; van Dalen, E.N.E.; Faessler, A.; Fuchs, C.; Gaitanos, T.; Grigorian, H.; Ho, A.; Kolomeitsev, E.E.; et al. Constraints on the high-density nuclear equation of state from the phenomenology of compact stars and heavy-ion collisions. *Phys. Rev. C* **2006**, *74*, 035802.
50. Most, E.R.; Motornenko, A.; Steinheimer, J.; Dexheimer, V.; Hanauske, M.; Rezzolla, L.; Stoecker, H. Probing neutron-star matter in the lab: Connecting binary mergers to heavy-ion collisions. *arXiv* **2022**, arXiv:2201.13150.
51. Adamczewski-Musch, J.; Arnold, O.; Behnke, C.; Belounnas, A.; Belyaev, A.; Berger-Chen, J.C.; Biernat, J.; Blanco, A.; Blume, C.; Böhmer, M.; et al. Probing dense baryon-rich matter with virtual photons. *Nat. Phys.* **2019**, *15*, 1040.
52. Stephanov, M.A.; Rajagopal, K.; Shuryak, E.V. Event-by-event fluctuations in heavy ion collisions and the QCD critical point. *Phys. Rev. D* **1999**, *60*, 114028.
53. Karsch, F. Lattice QCD at high temperature and density. *Lect. Notes Phys.* **2002**, *583*, 209.
54. Fukushima, K.; Hatsuda, T. The phase diagram of dense QCD. *Rept. Prog. Phys.* **2011**, *74*, 014001.
55. Halasz, A.M.; Jackson, A.D.; Shrock, R.E.; Stephanov, M.A.; Verbaarschot, J.J.M. On the phase diagram of QCD. *Phys. Rev. D* **1998**, *58*, 096007.
56. Blacker, S.; Bastian, N.U.F.; Bauswein, A.; Blaschke, D.B.; Fischer, T.; Oertel, M.; Soulтанis, T.; Typel, S. Constraining the onset density of the hadron-quark phase transition with gravitational-wave observations. *Phys. Rev. D* **2020**, *102*, 123023.
57. Blaschke, D.; Cierniak, M. Studying the onset of deconfinement with multi-messenger astronomy of neutron stars. *Astron. Nachr.* **2021**, *342*, 227.
58. Orsaria, M.G.; Malfatti, G.; Mariani, M.; Ranea-Sandoval, I.F.; García, F.; Spinella, W.M.; Contrera, G.A.; Lugones, G.; Weber, F. Phase transitions in neutron stars and their links to gravitational waves. *J. Phys. G* **2019**, *46*, 073002.
59. Cierniak, M.; Blaschke, D. Hybrid neutron stars in the mass-radius diagram. *Astron. Nachr.* **2021**, *342*, 819.
60. Kämpfer, B. Phase transitions in dense nuclear matter and explosive neutron star phenomena. *Phys. Lett. B* **1985**, *153*, 121.
61. Kämpfer, B. Phase transitions in nuclear matter and consequences for neutron stars. *J. Phys. G* **1983**, *9*, 1487.
62. Schertler, K.; Greiner, C.; Schaffner-Bielich, J.; Thoma, M.H. Quark phases in neutron stars and a 'third family' of compact stars as a signature for phase transitions. *Nucl. Phys. A* **2000**, *677*, 463.
63. Christian, J.E.; Zacchi, A.; Schaffner-Bielich, J. Classifications of Twin Star Solutions for a Constant Speed of Sound Parameterized Equation of State. *Eur. Phys. J. A* **2018**, *54*, 28.
64. Migdal, A.B.; Chernoutsan, A.I.; Mishustin, I.N. Pion condensation and dynamics of neutron stars. *Phys. Lett. B* **1979**, *83*, 158–160.
65. Kämpfer, B. On the collapse of neutron stars and stellar cores to pion-condensed stars. *Astrophys. Space Sci.* **1983**, *93*, 185–197.
66. Zdunik, J.L.; Haensel, P.; Schaeffer, R. Phase transitions in stellar cores, II Equilibrium configurations in general relativity. *Astron. Astrophys.* **1987**, *172*, 95.
67. Schaffner-Bielich, J. *Compact Star Physics*; Cambridge University Press: Cambridge, UK, 2020.
68. Buchdahl, H.A. General-relativistic fluid spheres. III. A static gaseous model. *Astrophys. J.* **1967**, *147*, 310.
69. Lattimer, J.M.; Prakash, M. Neutron star structure and the equation of state. *Astrophys. J.* **2001**, *550*, 426.
70. Dengler, Y.; Schaffner-Bielich, J.; Tolos, L. Second Love number of dark compact planets and neutron stars with dark matter. *Phys. Rev. D* **2022**, *105*, 043013.
71. Karkevandi, D.R.; Shakeri, S.; Sagun, V.; Ivanytskyi, O. Bosonic dark matter in neutron stars and its effect on gravitational wave signal. *Phys. Rev. D* **2022**, *105*, 023001.
72. Zdunik, J.L.; Haensel, P.; Schaeffer, R. Phase transitions in stellar cores, I Equilibrium configurations. *Astron. Astrophys.* **1983**, *126*, 121.
73. Alizzi, A.; Silagadze, Z.K. Dark photon portal into mirror world. *Mod. Phys. Lett. A* **2021**, *36*, 2150215.
74. Luzio, L.D.; Gavela, B.; Quilez, P.; Ringwald, A. Dark matter from an even lighter QCD axion: Trapped misalignment. *J. Cosmol. Astropart. Phys.* **2021**, *10*, 001.
75. Beradze, R.; Gogberashvili, M.; Sakharov, A.S. Binary Neutron Star Mergers with Missing Electromagnetic Counterparts as Manifestations of Mirror World. *Phys. Lett. B* **2020**, *804*, 135402.
76. Kobzarev, I.Y.; Okun, L.B.; Pomeranchuk, I.Y. On the possibility of experimental observation of mirror particles. *Sov. J. Nucl. Phys.* **1966**, *3*, 837.

77. Blinnikov, S.I.; Khlopov, M.Y. On the possible effects of “mirror” particles. *Sov. J. Nucl. Phys.* **1982**, *36*, 472.
78. Hodges, H.M. Mirror baryons as the dark matter. *Phys. Rev. D* **1993**, *47*, 456.
79. Goldman, I.; Mohapatra, R.N.; Nussinov, S. Bounds on neutron-mirror neutron mixing from pulsar timing. *Phys. Rev. D* **2019**, *100*, 123021.
80. Berezhiani, Z. Antistars or antimatter cores in mirror neutron stars? *arXiv* **2021**, arXiv:2106.11203.
81. Berezhiani, Z.; Bento, L. Neutron-mirror neutron oscillations: How fast might they be? *Phys. Rev. Lett.* **2006**, *96*, 081801.
82. Berezhiani, Z.; Comelli, D.; Villante, F.L. The Early mirror universe: Inflation, baryogenesis, nucleosynthesis and dark matter. *Phys. Lett. B* **2001**, *503*, 362–375.
83. Berezhiani, Z.; Gianfagna, L.; Giannotti, M. Strong CP problem and mirror world: The Weinberg-Wilczek axion revisited. *Phys. Lett. B* **2001**, *500*, 286–296.
84. Berezhiani, Z. Mirror world and its cosmological consequences. *Int. J. Mod. Phys. A* **2004**, *19*, 3775–3806.
85. Berezhiani, Z.; Biondi, R.; Mannarelli, M.; Tonelli, F. Neutron-mirror neutron mixing and neutron stars. *Eur. Phys. J. C* **2022**, *81*, 1036.
86. Schulze, R.; Kämpfer, B. Cold quark stars from hot lattice QCD. *arXiv* **2009**, arXiv:0912.2827.
87. Li, J.J.; Sedrakian, A.; Alford, M. Relativistic hybrid stars in light of the NICER PSR J0740+6620 radius measurement. *Phys. Rev. D* **2021**, *104*, L121302.
88. Ranea-Sandoval, I.F.; Han, S.; Orsaria, M.G.; Contrera, G.A.; Weber, F.; Alford, M.G. Constant-sound-speed parametrization for Nambu–Jona-Lasinio models of quark matter in hybrid stars. *Phys. Rev. C* **2016**, *93*, 045812.
89. Alford, M.G.; Han, S. Characteristics of hybrid compact stars with a sharp hadron-quark interface. *Eur. Phys. J. A* **2016**, *52*, 62.
90. Cierniak, M.; Blaschke, D. The special point on the hybrid star mass–radius diagram and its multi-messenger implications. *Eur. Phys. J. Spec. Top.* **2020**, *229*, 3663.